Bull. Mater. Sci., Vol. 36, No. 4, August 2013, pp. 613–618. © Indian Academy of Sciences.

Role of aluminium addition on structure of Fe substituted $Fe_{73.5-x}Si_{13.5}B_9Nb_3Cu_1Al_x$ alloy ribbons

GAUTAM AGARWAL, HIMANSHU AGRAWAL, M SRINIVAS[†], B MAJUMDAR[*,††] and N K MUKHOPADHYAY

Department of Metallurgical Engineering, Banaras Hindu University, Varanasi 221 005, India
[†]Naval Science and Technological Laboratory, Visakhapatnam 530 027, India
[††]Defence Metallurgical Research Laboratory, Hyderabad 500 058, India

MS received 20 June 2012; revised 6 August 2012

Abstract. **The investigation has dealt with the structure and magnetic properties of rapidly solidified and annealed $Fe_{73.5-x}Si_{13.5}B_9Nb_3Cu_1Al_x$ ($x = 0, 2, 4, 6$ at%) ribbons prepared by melt spinning. Complete amorphous structure was obtained in as-spun ribbons of $x = 0$ and 2 at% compositions, whereas structure of ribbons containing higher Al was found to be partially crystalline. Detailed thermal analyses of the alloys and the melt spun ribbons revealed that the glass forming ability in the form of T_x/T_l (ratio between crystallization and liquidus temperature) is the highest for 2 at% Al alloys and decreases with further addition of Al. Annealing of all as spun ribbons resulted in the precipitation of nanocrystalline phase embedded in amorphous matrix in the form of either DO_3 phase or *bcc* α-Fe(Si/Al) solid solution depending on the initial composition of the alloy. Only *bcc* α-Fe(Si/Al) solid solution was formed in 2 at% Al ribbons whereas ordered DO_3 structure was found to be stabilized in other ribbons including 0 at% Al. A detailed study on determination of precision lattice parameter of nanocrystalline phase revealed that the lattice parameter increases with the addition of Al indicating the partitioning behaviour of Al in nanocrystalline phase.**

Keywords. **Rapid solidification; amorphous; nanocrystalline; glass forming ability; Finemet; soft magnetic properties.**

1. Introduction

Nanocrystalline Fe–Si–B–Nb–Cu alloy systems, popularly known as FINEMET were first developed by Yoshizawa *et al* (1988) and Yoshizawa and Yamauchi (1989) at Hitachi Metal Corporation in Japan. The ultra-soft magnetic characteristics such as high permeability (10^5), low coercivity (0·005 Oe) and high saturation induction (up to 1·3 T) arise in these alloys because of the nanocrystalline phase embedded in amorphous matrix (Yoshizawa and Yamauchi 1990). The composition of most widely studied FINEMET alloy systems is $Fe_{73.5}Si_{13.5}B_9Nb_3Cu_1$ because it shows the best combination of soft magnetic properties. These nanocrystalline alloys are prepared by partial devitrification of precursor amorphous phase which is produced through rapid solidification (melt spinning).

In recent years, efforts have been devoted to further improve the soft magnetic properties of Finemet alloys by either modifying the processing conditions during melt spinning (Srinivas *et al* 2011a) and heat treatment (Majumdar and Akhtar 2005) or partially substituting different constituent elements (Franco *et al* 2000; Ma *et al* 2007; Monata *et al* 2009). It has been observed that the annealed ribbons, processed at higher wheel speed during melt spinning exhibit higher volume fraction of the nanocrystalline phase which results in improved soft magnetic properties (Srinivas *et al* 2011a). However, processing the ribbons at higher initial melt temperature decreases the glass forming ability of the alloys and results in deteriorating the soft magnetic properties (Srinivas *et al* 2011b).

Of many elements added to Finemet, substitution of small amount of Al in place of Fe/Si was found to reduce magnetocrystalline anisotropy and hence coercivity (Zorkovska *et al* 2000). Lim *et al* (1993) first reported that the addition of 1 at% Al reduced the coercivity of the annealed ribbons. Tate *et al* (1998) further studied compositions containing Al up to 10% and found the minimum coercivity (as low as 0·3 A/m) in the optimally heat-treated 2–8 at% Al compositions due to the decrease of magnetocrystalline anisotropy. A zero magnetostriction value is found in 2 at% Al composition which resulted in the best soft magnetic properties. Several other reports also confirmed that the minimum coercivity in 2% Al composition (Frost *et al* 1999; Todd *et al* 2000). Zorkovska *et al* (2000) reported that small amounts of Al (up to 3%) do not significantly reduce the saturation magnetization; the decrease being markedly at higher Al content due to the formation of paramagnetic phases. However, a systematic study on the evolution of structure of Al added Finemet alloys and its effect on soft magnetic properties has

*Author for correspondence (bhaskar@dmrl.drdo.in)

not been investigated in detail. Therefore, the present investigation is focused on studying the glass forming behaviour of melt spun $Fe_{73.5-x}Al_xSi_{13.5}B_9Nb_3Cu_1$ ribbons. The structure of nanocrystalline phase during annealing of the ribbons have been evaluated and correlated with the magnetic property.

2. Experimental

Alloys of nominal composition, $Fe_{73.5-x}Al_xSi_{13.5}B_9Nb_3Cu_1$ (x = 0, 2, 4 and 6 at%), were prepared using a vacuum arc melting furnace. Alloys are termed as Al0, Al2, Al4 and Al6. Table 1 shows nomenclature and corresponding nominal composition of the alloys. Approximately 10 g of each alloy was rapidly solidified to make amorphous ribbon of 30–40 μm thickness using a vacuum melt spinner at a wheel speed of 41 m/s, melt pouring temperature of 1250–1300 °C and ejection pressure of 0·35 kgf/cm^2. For partial nanocrystallization, all ribbons were annealed just above the onset of crystallization temperature in a vacuum tubular furnace (2×10^{-5} mbar) for 1 h.

Structure of the as spun and annealed ribbons was determined by X-ray diffractometer (PHILIPS PW1830 Model) using CuKα (λ = 1·54056 Å) radiation. A differential thermal analyser (TA-1600) was used to evaluate thermal stability of the as quenched ribbons. A transmission electron microscope (TEM) (Model: FEI Tecnai-20 G^2) has been employed to investigate detailed microstructural features of as-spun and annealed ribbons. The samples for TEM investigation have been prepared using a precision ion polishing system (PIPS) by thinning from both sides of the ribbon. A vibrating sample magnetometer (VSM) (ADE EV7 Model) was employed to obtain saturation magnetization with an applied field of up to 20 kOe.

3. Results and discussion

XRD patterns of all as-spun ribbons, processed under similar conditions are shown in figure 1. It can be observed that the as spun Al0 and Al2 ribbons show broad halo peaks confirming the formation of completely amorphous phase whereas Al4 and Al6 show sharp and intense peaks superimposed on broad halo confirming partial crystallization. The presence of superlattice peaks around 2θ = 28° and 31° in the as spun Al6 ribbon confirms the existence of DO_3 structure.

Table 1. Nomenclature and composition of Al substituted alloys and their different characteristics.

Sl. no.	Nomenclature	Nominal composition	T_x (°C)	T_s (°C)	T_l (°C)	T_x/T_l	a_o (Å)
1.	Al0	$Fe_{73.5}Si_{13.5}B_9Nb_3Cu_1$	510	1100	1186	0·43	5·660
2.	Al2	$Fe_{71.5}Si_{13.5}B_9Nb_3Cu_1Al_2$	555	1111	1173	0·47	5·689 (Fe_3Si) 2.8445 (α-FeSi)
3.	Al4	$Fe_{69.5}Si_{13.5}B_9Nb_3Cu_1Al_4$	494	1110	1185	0·42	5·692
4.	Al6	$Fe_{67.5}Si_{13.5}B_9Nb_3Cu_1Al_6$	490	1117	1186	0·41	5·701

T_x, crystallization temperature; T_s, solidus temperature T_l, liquidus temperature and a_o, precision lattice parameter.

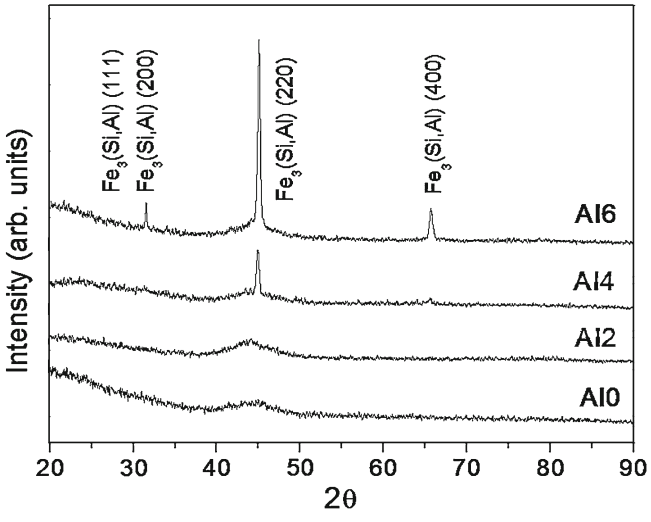

Figure 1. XRD patterns of as spun ribbons.

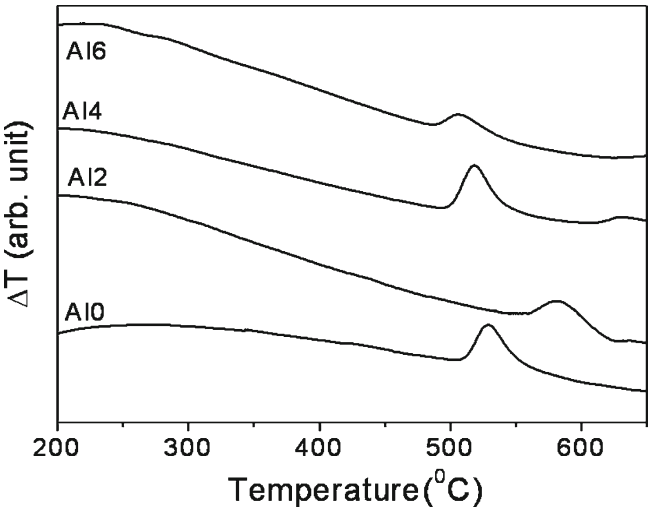

Figure 2. DSC thermograms of as spun ribbons.

Figure 2 shows DSC thermograms of all as-spun ribbons scanned up to 650 °C, revealing the exothermic peaks corresponding to the crystallization of the amorphous phase. The crystallization temperatures (T_x) are also tabulated in table 1. It can be observed that the T_x temperature increases with the addition of Al up to 2 at% as compared to the Finemet composition (Al0) and then decreases further. Further reduction of crystallization temperature beyond 2 at% Al may also be attributed to the presence of partial crystalline phase which changes the composition of remaining amorphous matrix.

All the melt spun ribbons were annealed for 1 h at the temperature, just above the primary crystallization temperature of the respective ribbons (based on DSC thermograms as shown in figure 2). X-ray diffraction patterns of annealed ribbons are shown in figure 3. It is interesting to observe that in case of Al0 ribbon, Fe_3Si phase having DO_3 structure is precipitated out which can be confirmed from the presence of superlattice peaks at around $2\theta = 28°$ and 31°, whereas only α-*bcc* solid solution can be indexed in annealed Al2 ribbons. With further increase of Al content, precipitation of DO_3 phase is evident in annealed A4 and A6 ribbons.

The precision lattice parameters (a_o) of crystalline phases (Fe_3Si for Al0, Al4 and Al6 and α-*bcc* solid solution for Al2) for all annealed ribbons have been determined using Nelson Riley (N–R) extrapolation method in which lattice parameter, calculated from each peak is plotted against the N–R function, $((\cos^2\theta/\sin\theta) + (\cos^2\theta/\theta))$ (Cullity 1979). A typical plot of the precision lattice parameters (a_o) as a function of N–R function for annealed Al0 ribbon is shown in figure 4. A straight line is drawn by regression analysis and extrapolated up to zero value of N–R function. The intercept value gives measure of the precision lattice parameter. Table 1 gives precision lattice parameter values of different annealed ribbons. It can be clearly observed that the a_o of DO_3 phase increases with Al content.

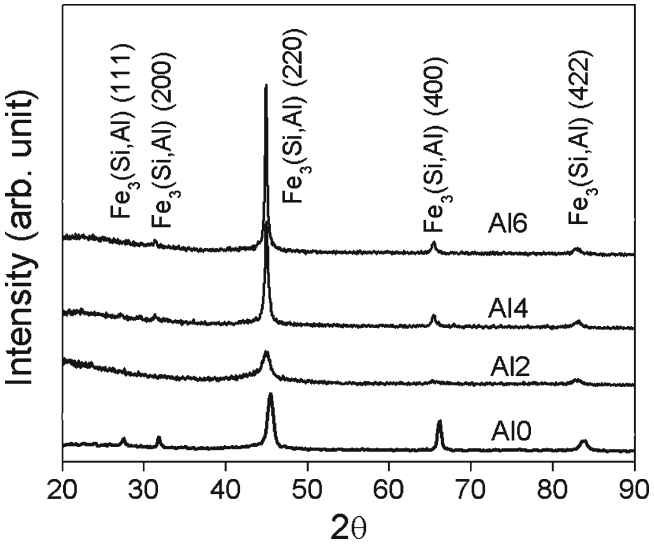

Figure 3. XRD patterns of annealed ribbons.

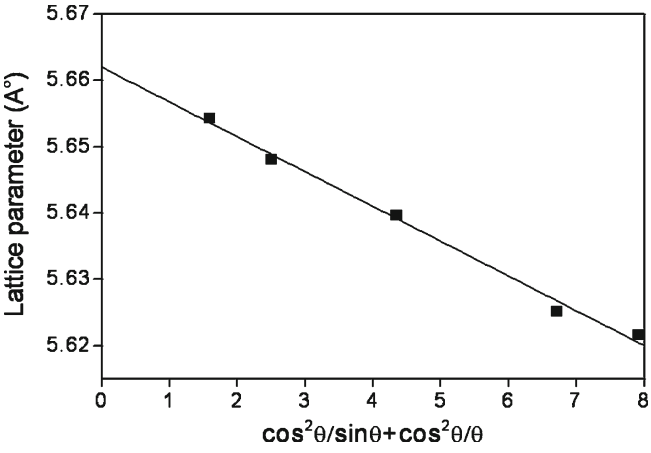

Figure 4. Lattice parameter as a function of N–R function for annealed Al0 ribbon.

Figure 5 shows series of TEM bright field images and corresponding selected area diffraction (SAD) patterns (inset) of annealed Al0, Al2 and Al6 ribbons exhibiting nanocrystalline precipitates in amorphous matrices. In case of Al0 ribbons (figure 5(a)), uniform grain size of nanocrystalline phase is in the order of 15 nm which is in agreement with the earlier TEM observations in similar alloys (Majumdar and Akhtar 2005). The presence of superlattice rings (inset of figure 5(a)) corresponding to (111) and (200) reflections is the indication of ordered Fe_3Si phase. In case of Al2 ribbon (figure 5(b)), grain size is <20 nm. The absence of ordered peaks (inset of figure 5(b)) indicates that the nanocrystalline phase formed is *bcc* α-Fe–Si(Al) solid solution. This corroborates with the results observed in the XRD patterns (figure 3). The microstructure of Al6 ribbon (figure 5(c)) exhibits a bimodal grain size distribution; a few big particles of 300–600 nm and mostly medium range particles of around 50 nm. The bottom inset in figure 5(c) is the SAD pattern taken from the nanocrystalline region whose average size is 50 nm and indicates the formation of DO_3 phase. High magnification bright field image of globular grain (size, ~550 nm) reveals cellular morphology which implies that the grain was formed during rapid solidification. The inset shows the single crystal diffraction pattern obtained from the globular grain taken during the diffraction condition at a zone axis of {001} of DO_3 phase.

The saturation magnetization ($4\pi M_s$) of the annealed ribbons as a function of Al content is shown in figure 6. It is interesting to observe that the $4\pi M_s$ value is less in 2 at% Al ribbon (Al2) as compared to the Finemet composition (Al0) and further rises when the Al content in the alloy is 4 at% (Al4). The saturation magnetization again decreases for 6 at% Al (Al6) ribbon.

Our results indicate that during melt spinning under similar processing conditions, fully amorphous phase was formed in Al0 and Al2 alloys, whereas further increase of Al content led to the precipitation of crystalline phase. In order to understand the reason for obtaining fully amorphous phase

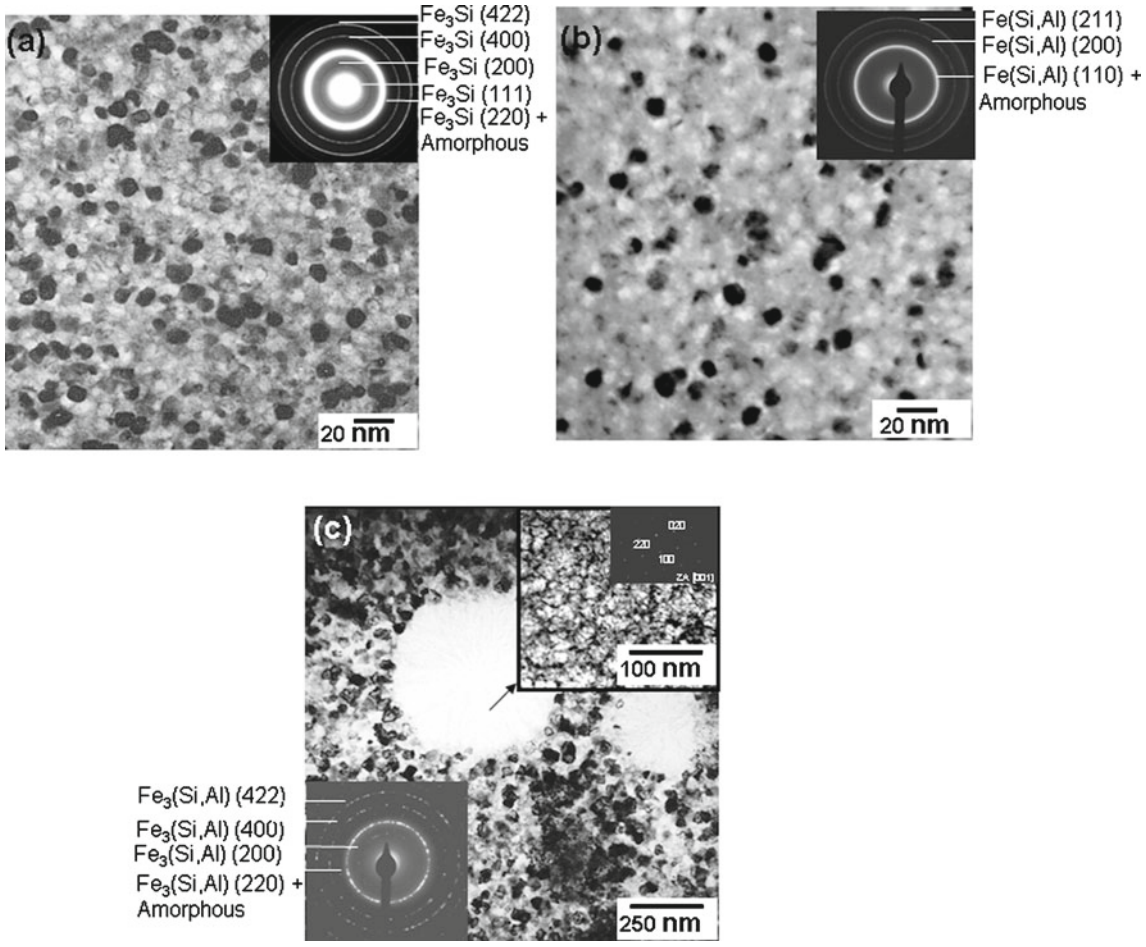

Figure 5. TEM images of (**a**) Al0, (**b**) Al2 and (**c**) Al6 annealed ribbons (insets: corresponding SAD patterns).

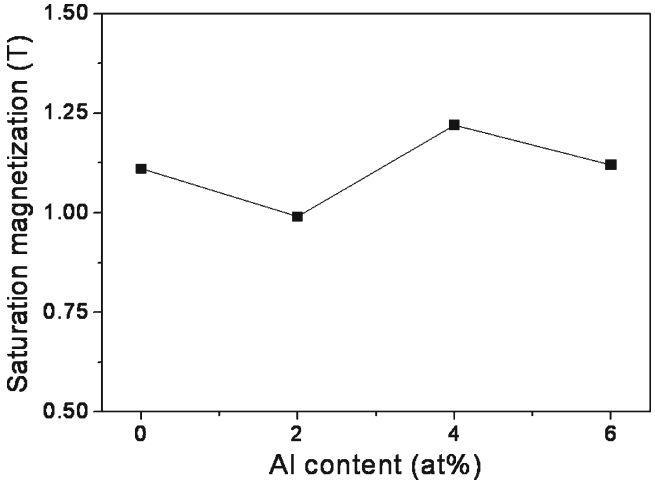

Figure 6. Saturation magnetization of annealed ribbons as a function of Al content.

in Al0 and Al2 alloys, the glass forming ability (GFA) of all alloys has been determined based on the ratio of crystallization to liquidus temperature (T_x/T_l) (Mondal and Murty 2005). Detailed differential thermal analyses (DTA) at a heating rate of 20 °C/min have been carried out to obtain the melting behaviour of all cast alloys. The thermograms of all the alloys are shown in figure 7. The liquidus temperature (T_l) has been obtained from the finish of melting peak from each thermogram and tabulated in table 1. GFA of each alloy in the form of T_x/T_l has been calculated and given in table 1. It can be clearly observed that the glass forming ability is high for Al2 alloy and next is Al0 alloy.

Annealing of all ribbons leads to the precipitation of nanocrystalline phase from the precursor amorphous matrix. Both XRD and TEM results confirm that the precipitated nanocrystalline phase is either DO_3 phase or *bcc* α-Fe(Si/Al) solid solution depending on the initial composition of the alloy. The *bcc* α-Fe(Si/Al) solid solution was found to be stabilized with increasing Al up to 2 at% as compared to the ordered DO_3 structure of Fe_3Si phase in 0 at% Al ribbon (Al0). Further increase in Al content again stabilizes the ordered $Fe_3(Si, Al)$ phase. In fact, high crystallization temperature of Al2 sample as compared to the other samples may be attributed to the formation of *bcc* solid solution which has higher thermal stability than that of DO_3–Fe_3Si phase.

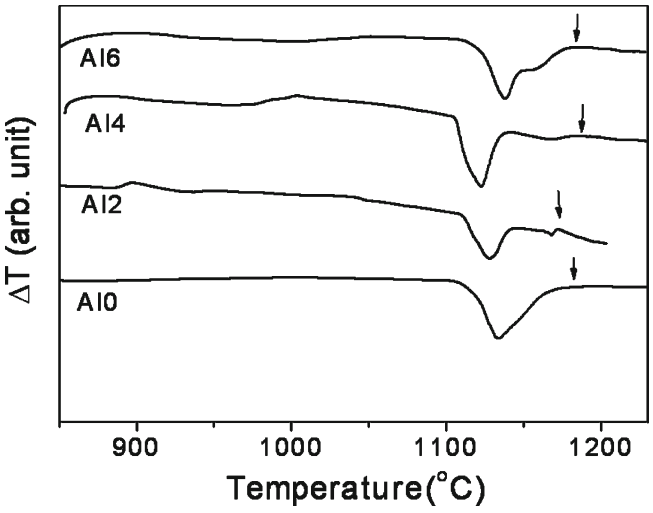

Figure 7. DTA thermograms of as cast alloys.

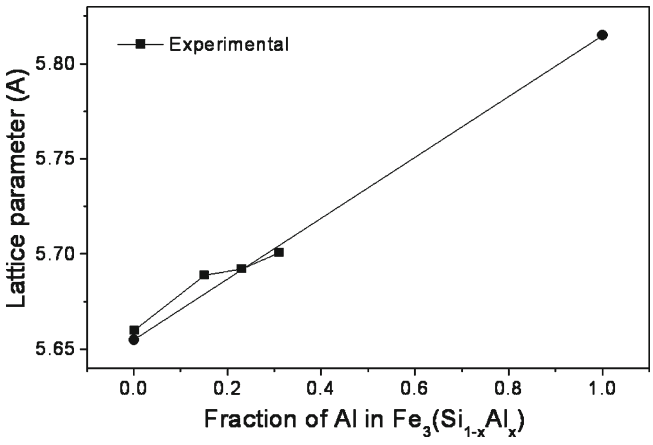

Figure 8. Variation of lattice parameter with Al content.

The increase in lattice parameters (a_o) of crystalline phases with Al content (table 1) is possibly due to the dissolution of Al atoms in the crystalline phase. Al atoms (atomic radius, 1·82 Å) tend to expand the lattice of Fe (atomic radius, 1·72 Å) while Si atoms (atomic radius, 1·46 Å) cause it to shrink. Similar results on increasing the lattice parameter of annealed Finemet alloys with the addition of Al and Ge have been observed elsewhere (Shahri *et al* 2007). The result is also in agreement with the earlier observation where a detailed 3-dimensional atom probe analysis of annealed $Fe_{73.5}Al_2Si_{13.5}B_9Nb_3Cu_1$ ribbons reported by Warren *et al* (1999) revealed that almost 90% of Al is preferentially partitioned to the Fe–Si nanocrystalline phase over amorphous matrix.

Considering that all Al added to the alloy is present only in the nanocrystalline phase after annealing, the fraction of Al present in ordered DO_3 Fe_3(Si, Al) has been calculated based on the composition of the alloys. In case of Al2 composition, the lattice parameter of Fe_3(Si, Al) can be taken as double of the *bcc* α phase (in terms of pseudo-cubic cell) (Pearsons 1964). Figure 8 shows the precision lattice parameter as a function of fraction of Al present in Fe_3(Si, Al) phase. The lattice parameters of pure Fe_3Si (fraction of Al is zero) and Fe_3Al (fraction of Al is 1) are also indicated in the figure (Pearsons 1964). A straight line conforming to the Vegard's law of lattice parameter is drawn by joining a_o of Fe_3Si and Fe_3Al. It can be observed that a_o of Fe_3(Si, Al) for all alloys studied almost coincides with the line, except for 2 at% Al alloy which shows a higher value than expected, based on Vegard's law. In case of ordered Fe_3(Si, Al) structure, Si sites are gradually replaced by Al atoms with increasing Al content of the alloy and therefore, follows Vegard's law of mixing. Since α-Fe *bcc* solid solution was formed in Al2 ribbon (as confirmed from XRD and TEM), Al atoms probably substitute Fe atoms and since atomic radius of Al is bigger than that of Fe, one can expect a larger unit cell of the *bcc* solid solution as compared to ordered Fe_3(Si, Al) structure. Therefore, it can be concluded that the assumption, that all Al atoms present in DO_3 structure holds good for the present investigation.

The cellular morphology of submicron-sized grains (~500 nm) in Al6 ribbon, observed in TEM (in figure 5(c)) is evidence of primary solidification from the amorphous phase. It can be noted that although DO_3 phase has been formed both during melt spinning and annealing, there exists a distinct size difference between those grains; the grains formed during rapid solidification is an order of magnitude larger than that formed during annealing. Similar results have been observed elsewhere in $Fe_{88}Zr_7B_4Cu_1$ alloy where size of *bcc* α-Fe phase obtained during melt spinning is very large as compared to nanocrystalline *bcc* α-Fe phase obtained after annealing the same sample (Arvindha Babu *et al* 2008).

The variation of saturation magnetization ($4\pi M_s$) values with Al content can be correlated with the presence of phases in all ribbons. Both amorphous and crystalline phases contribute towards the saturation magnetization of annealed ribbon as per the equation (Shahri *et al* 2007):

$$M_s = v \times M_s^{amor} + (1 - v)\, M_s^{cryst},$$

where M_s^{amor} and M_s^{cryst} are the saturation magnetization of amorphous and crystalline phases, respectively, and v the volume fraction of amorphous phase. Since Al preferentially partitioned to the crystalline Fe–Si phase, it can be approximated that the presence of Al in crystalline phase would influence the saturation magnetization values.

The initial reduction of $4\pi M_s$ up to 2 at% Al may be due to the dilution of ferromagnetic Fe with Al atoms which preferentially occupy Fe sites in *bcc* α-Fe phase. Recently, Christensen *et al* (2008) reported that the theoretical and experimental sublattice moments of Fe_3Al and Fe_3Si in Bohr magnetons (μB) per atom and shown that magnetic moment of different point symmetry of the [A], [B], [C] and [D] sites of the DO_3 structure varies depending on the site occupancy of Fe/Si/Al atoms in the sublattice. Sites [A], [B] and [C] are occupied with Fe atoms, whereas Si/Al atoms occupy *D* sites. Since the Fe[A] and Fe[C] sites have tetrahedral point

symmetry with four Fe[B] and four Si[D] or Al[D] nearest neighbours, the interactions between Si/Al with Fe will dictate the magnetic moment of these sites. It has been observed that the Fe[A] and Fe[C] sites of Fe_3Al possess higher Bohr magneton as compared to that of Fe_3Si because of magnetovolume effect. Therefore, when ordered Fe_3(Si, Al) is precipitated out from amorphous phase, one can expect the increase of magnetic moment as compared to Fe_3Si because of replacement of Si with Al. The decrease in magnetization beyond 4 at% Al may be attributed to the Fe atoms being substituted by Al. Further, Mössbauer spectroscopy study is necessary to experimentally evaluate the site occupancy of different atoms in DO_3 phase and α-*bcc* solid solution.

4. Conclusions

(I) Completely amorphous phase was formed in ribbons up to 2 at% Al, where ribbons containing higher Al were found to be partially crystalline. The results can be explained from the calculated glass forming ability (GFA) in the form of T_x/T_l (ratio between crystallization and liquidus temperature), which shows highest value for 2 at% Al alloys and decreases with further addition of Al.

(II) Annealing of as-spun ribbons resulted in the precipitation of only *bcc* α-Fe(Si, Al) solid solution in 2 at% Al ribbons, whereas ordered DO_3 structure was found to be stabilized in other ribbons including 0 at% Al. The increase of precision lattice parameter with Al confirms the partitioning behaviour of Al in nanocrystalline phase.

(III) The size of the nanocrystalline grains increases with Al addition. In case of higher Al content ribbon, such as Al6, although DO_3 phase has been formed during both melt spinning and annealing, there exists a distinct size difference between those grains; the grains formed during rapid solidification is an order of magnitude larger than that formed during annealing.

(IV) The lower saturation magnetization value ($4\pi M_s$) of the annealed 2 at% Al ribbon as compared to the Al0 composition may be due to the partitioning of Al atom at ferromagnetic Fe sites. The value again increases for 4 at% Al due to higher magnetic moment of the ordered DO_3 Fe_3(Si, Al) phase as compared to Fe_3Si. Further decrease of magnetization beyond 4 at% Al may be due to the dilution of Fe atoms by Al.

Acknowledgements

The authors would like to acknowledge the help rendered by Dr S Pandian for melting the alloys, Dr A K Singh for XRD and Mr Rajdeep Sarkar for transmission electron microscopy. Thanks are due to Dr G Malakondaiah, Director, DMRL, for his kind support.

References

Arvindha Babu D, Majumdar B, Sarkar R, Akhtar D and Chandrasekaran V 2008 *J. Phys. D: Appl. Phys.* **41** 195002

Christensen N E, Kudrnovský J and Rodriguez C O 2008 *Int. J. Nanoelectron. Mater.* **1** 1

Cullity B D 1979 *Elements of X-ray diffraction* (Massachusetts: Addison-Wesley Publishing Company)

Frost M, Todd I, Davies H A, Gibbs M R J and Major R V 1999 *J. Magn. Magn. Mater.* **203** 85

Franco V, Conde C F, Conde A, Varga B and Lovas A 2000 *J. Magn. Magn. Mater.* **215–216** 404

Lim S H, Pi W K, Noh T H, Kim H J and Kang I K 1993 *J. Appl. Phys.* **73** 6591

Ma Z, Wang Z, Han X, Yin X and Wang B 2007 *Mater. Sci. Eng.* **A448** 216

Majumdar B and Akhtar D 2005 *Bull. Mater. Sci.* **28** 395

Mondal K and Murty B S 2005 *J. Non-Cryst. Solids* **351** 1366

Monata M E, Brzozowaski R, Wasaik M and Uznanski P 2009 *Nucl. Instrum. Meth. Phys. Res.* **B267** 414

Pearsons W B 1964 *Handbook of lattice spacing and structure of metals and alloys* (Oxford: Pergamon)

Shahri F, Beitollahi A, Shabestari S G and Kamali S 2007 *Phys. Rev.* **B76** 024434

Srinivas M, Majumdar B, Akhtar D, Srivastava A P and Srivastava D 2011a *J. Mater. Sci.* **46** 616

Srinivas M, Majumdar B, Phanikumar G and Akhtar D 2011b *Metall. Mater. Trans.* **B42** 370

Tate B J, Parmar B S, Todd I, Davies H A, Gibbs M R J and Major R V 1998 *J. Appl. Phys.* **83** 6335

Todd I, Tate B J, Davies H A, Gibbs M R J, Kendall D and Major R V 2000 *J. Magn. Magn. Mater.* **215–216** 272

Warren P J, Todd I, Davies H A, Cerezo A, Gibbs M R J, Kendall D and Major R V 1999 *Scr. Mater.* **41** 11

Yoshizawa Y and Yamauchi K 1989 EU patent no. 0299498

Yoshizawa Y and Yamauchi K 1990 *Mater. Trans. JIM* **31** 307

Yoshizawa Y, Oguma S and Yamauchi K 1988 *J. Appl. Phys.* **64** 6044

Zorkovska A, Muzminski M, Fuzer J, Kollar P and Svec T 2000 *J. Magn. Magn. Mater.* **215–216** 459